Inorganic Chemistry

Article

pubs.acs.org/IC

Crystal Structure, Electronic Structure, and Photoluminescence Properties of $La_3BW_{1-x}Mo_xO_9:Eu^{3+}$ Red Phosphor

Jinping Huang,* Binghu Hou, Hongya Ling, Jie Liu, and Xibin Yu

Shanghai Key Laboratory of Rare Earth Functional Materials, Department of Chemistry, Shanghai Normal University, Shanghai 200234, People's Republic of China

Supporting Information

ABSTRACT: A series of $La_3BW_{1-x}Mo_xO_9:Eu^{3+}$ (x = 0–0.4) polycrystalline powders were prepared by using solid-state reactions. The phase structure, UV–vis absorption spectra, and photoluminescence properties were studied as a function of the Mo/W ratio. When Mo^{6+} ions are incorporated into the lattice, the characteristic sharp lines in the excitation spectra of Eu^{3+} monitored at 617 nm are prominently enhanced, which join the ligand-to-metal charge transfer (LMCT) band of $La_3BW_{1-x}Mo_xO_9:Eu^{3+}$ into a broad band ranging from 250 to 450 nm centered at 375 nm. The intensity of the broad excitation band reaches a maximum when the content of Mo^{6+} ions increases to x = 0.3. On the other hand, the LMCT band around 306 nm decreases and shifts toward the longer wavelength. These features are advantageous to near-UV or blue light GaN-based LED applications. Orbital population analysis by density functional theory calculation (DFT) reveals that the near-UV excitation of $La_3BW_{1-x}Mo_xO_9:Eu^{3+}$ red phosphor is due to the electronic transition from the O 2p orbital to the W 5d and Mo 4d orbitals, respectively. With the introduction of Mo^{6+} into the lattice, the band gap of $La_3BW_{1-x}Mo_xO_9$ becomes narrower than that of the pure phase La_3BWO_9.

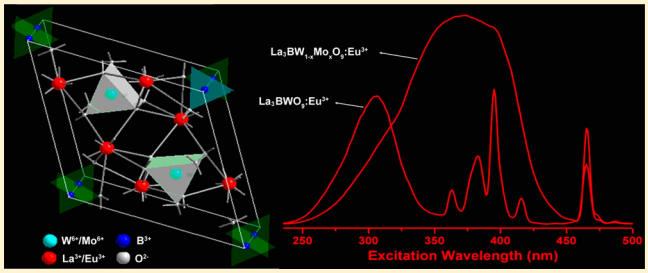

1. INTRODUCTION

During the past decade, continuing improvements in the efficiency of white light emitting diodes (WLED) have pointed to the tremendous potential of energy savings in general lighting applications.[1−3] Based on the technology to produce white light by combining a near-UV or blue light emitting diode (LED) chip with a downconversion phosphor,[4,5] the eventual performances of WLED devices mainly depend on the phosphors. Primarily, the excitation wavelength of the phosphor should fall in the near-UV or blue light region and thus, a high wavelength conversion efficiency can be achieved by LED chips on the market. Up to now, in comparison with blue and green phosphors, the existing red phosphors still show some limitations in terms of red color purity, efficiency, and stability, which directly result in poor luminous efficiency and color rendering index of the WLED lighting system.[6−8] Therefore, the search for novel red phosphors with high efficiency, excellent chemical stability, and effective absorption in the blue or UV region is an urgent task.

Recently, tungstate and molybdate phosphors for LED applications have attracted much attention due to the high chemical–physical stability, low synthetic temperature, and environmentally friendly characteristics.[9−11] In addition, these materials have a broad and an intense ligand-to-metal charge transfer (LMCT) band in the UV or near-UV region, which is expected to capture the emission from a GaN-based LED in this range.[12] For Eu^{3+} ion activated tungstate and molybdate compounds, the energy is transferred to the activator ions from the host lattice by a nonradiative mechanism and the red emission derived from the $^5D_0$–$^7F_2$ transition of Eu^{3+} is enhanced when the ion is located in a noncentrosymmetric site.[13]

The current investigations have been conducted to further improve the luminescence performance of tungstates and molybdates as red phosphors. Because the excitation bands of $W(Mo)O_4$ groups are generally in the UV region, near-UV or blue light cannot be efficiently utilized by the host lattices. In addition, for Eu^{3+}-activated phosphors, the excitation efficiencies are generally limited to the intrinsically spin and parity forbidden f–f transitions of Eu^{3+} ions. As is in centrosymmetric sites, Eu^{3+} ion emission is usually dominated by orange light. Improvements have focused on either partially substituting the tungsten of phosphors with heterogeneous metal ions (such as Mo^{6+} and Si^{4+} ions)[14] to modify the coordination environment of the Eu^{3+} luminescence center or doping them with sensitizer ions (such as Bi^{3+} and Li^+) to better utilize near-UV or blue excitation from LED chips.[10,11] On the basis of these strategies, Cheetham et al.[15,16] prepared a series of novel red phosphors including $NaM(WO_4)_{2-x}(MoO_4)_x:Eu^{3+}$ (M = Gd, Y, Bi) by partially substituting MoO_4^{2-} for WO_4^{2-}. As a consequence, the charge transfer band of the phosphors from the UV region shifts toward longer wavelengths, making the luminescent system suitable for LED devices in which the excitation is

Received: March 30, 2014
Published: August 22, 2014

   dx.doi.org/10.1021/ic500748c | Inorg. Chem. 2014, 53, 9541–9547

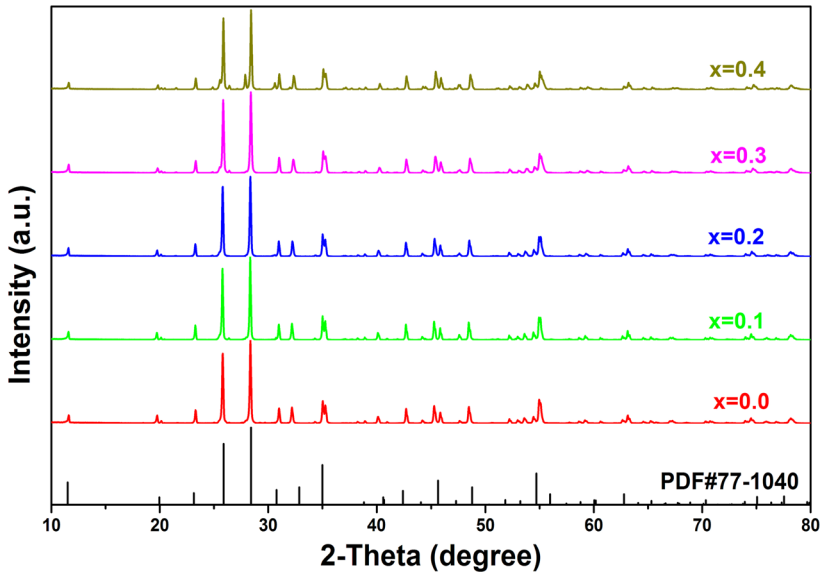

Figure 1. XRD patterns of $La_{2.7}BW_{1-x}Mo_xO_9$:0.3Eu^{3+} incorporated with different contents of Mo^{6+}.

within the near-UV or blue light range. Under excitation at about 400 nm, excellent efficiency of the red emission was obtained. Similarly, Li[17] and Tian[11] investigated the system $Ba_2MgW(Mo)O_6$:Eu^{3+} by partial substitution of Mo^{6+} for W^{6+} and Y_2WO_6:Eu^{3+} incorporated with Mo^{6+} or Bi^{3+}, respectively. Both groups found that the energy transfer efficiency of WO_6 → Eu^{3+} could be greatly enhanced. On the other hand, Liu et al.[18] reported that, by introduction of Si^{4+} into the lattice of $LiEuMo_2O_8$, the red emission of $LiEuMo_{2-x}Si_xO_8$ phosphor was improved by 30% at x = 0.2 under 395 nm excitation. The authors proposed that doping Si^{4+} ion caused the distortion and slight shrinking of the unit cell of the $LiEuMo_2O_8$ material, which resulted in a blue shift of the LMCT band and ultimately enhanced the excitation efficiency of $LiEuMo_2O_8$ in the spectral region of 360−400 nm.

Rare earth borotungstates with the general formula Ln_3BWO_9 were found to be promising luminescent and nonlinear optical materials.[19−21] The hexagonal noncentrosymmetric structure of the $P6_3$ space group (No. 173) has been confirmed by single-crystal X-ray diffraction in which the single sites are occupied by [BO_3], [WO_6], and Ln^{3+} ions.[22−24] Our work gives insight into the modulation of the excitation wavelength of Eu^{3+}-doped borotungstate red phosphor for LED applications. Although MoO_6 is generally used to substitute WO_6 to adjust the LMCT band of a tungstate phosphor because of the isomorphism effect,[14,17] this strategy is not always suitable for all tungstate systems. For some tungstate compounds, introduction of Mo^{6+} will lead to collapse of the structure and, eventually, the quenching of the luminescence of the phosphor. Zhang et al.[25] incorporated Mo^{6+} into double perovskite $NaGdMg(W, Mo)O_6$ red phosphor via annealing metal ion complex precursors by accurate control of reaction conditions.

Here, we report incorporation of Mo^{6+} into rare-earth borotungstates by a facile solid-state reaction. The influence of Mo^{6+} and the Mo/W ratio on the structure and photoluminescence properties of $La_3BW_{1-x}Mo_xO_9$:Eu^{3+} are investigated by excitation and emission spectra, UV−vis absorption spectra, crystal structure analysis, and density functional theory (DFT) calculations.[26] Detailed information about the arrangement of atoms and orbital population obtained by DFT calculations may help to understand the structure−property relationship, which is fundamental in the design of novel red phosphors applied in WLED.

2. EXPERIMENTAL AND CALCULATION METHODS

2.1. Synthesis. The red phosphors $La_3BW_{1-x}Mo_xO_9$:Eu^{3+} were prepared by solid-state reactions. The starting materials La_2O_3 (99.99%), Eu_2O_3 (99.99%), WO_3 (99.0%), MoO_3 (99.0%), and H_3BO_3 (99.5%) were weighed according to the stoichiometric ratio. These powders were mixed thoroughly using an agate mortar. Then, the homogeneous mixture was filled into a corundum crucible. After annealing under 650 °C for 6 h and continuously increasing the temperature to 1100 °C and holding this temperature for another 12 h, a white product was obtained when it was reduced to room temperature naturally.

2.2. Characterization. The compositions were determined by energy dispersive X-ray spectroscopy (EDS) attached to a field scanning electron microscope (JSM-6700F). The phases were identified by powder X-ray diffraction (XRD) measurements on a Bragg−Brentano diffractometer (Rigaku D/Max-2200) with a Rint 2000 wide angle goniometer using monochromated Cu Kα radiation (λ = 1.5418 Å) of a graphite curve monochromator at 40 kV and 30 mA. The XRD Rietveld refinement was performed by using the GSAS suite program,[27] and the data were collected over a 2θ range from 10 to 100° at intervals of 0.02° with a counting time of 15 s/step. UV−vis absorption spectra were recorded on a UV−vis spectrophotometer (JASCO V-670). The excitation and emission spectra were measured on a fluorescence spectrophotometer (Photon Technology International) equipped with a 60 W Xe-arc lamp as the excitation light source. All measurements were taken at room temperature under identical conditions.

2.3. Details of the Calculation. The doped sample of $La_3BW_{0.7}Mo_{0.3}O_9$ was selected for DFT analysis by using the CASTEP code.[26] A sample of the hexagonal host lattice La_3BWO_9 was also calculated for comparison. Geometry optimization and calculation of properties were performed to determine the crystal structure, electronic structure, and orbital population. For both compositions, the Vanderbilt ultrasoft pseudopotential with a cutoff energy of 300 eV was used, and k-points of 3 × 3 × 4 were generated by using the Monkhorst−Pack scheme.[28] The exchange and correlation functions were treated by the local density approximation (LDA) in the formulation of CA-PZ.[29,30] During the geometry optimization, lattice parameters and atomic positions were optimized simultaneously. For the self-consistent field iterations, the convergence tolerance for geometry optimization was selected with the differences in total

dx.doi.org/10.1021/ic500748c | Inorg. Chem. 2014, 53, 9541−9547

energy, the maximal ionic Hellmann−Feynman force, the stress tensor, and the maximal displacement being within 5.0×10^{-6} eV/atom, 1.0×10^{-2} eV/Å, 2.0×10^{-2} GPa, and 5.0×10^{-4} Å, respectively.

3. RESULTS AND DISCUSSION

3.1. Structure Characterization. A series of samples of $La_{2.7}BW_{1-x}Mo_xO_9$:$0.3Eu^{3+}$ with different ratios of Mo to W (x = 0−0.4) have been prepared in order to optimize the luminescent properties. Powder XRD patterns in Figure 1 show that all the as-prepared samples are identical and match well with those of the pure rare earth borotungatates La_3BWO_9 (PDF# 77-1040). Until the content of Mo^{6+} increases to x = 0.3, no diffraction peak of impurity is detected, indicating that introduction of Mo^{6+} into the lattice does not cause a significant change of structure, and the single phase $La_3BW_{1-x}Mo_xO_9$:Eu^{3+} can exist up to x = 0.3. When x > 0.3, the impurity lanthanum tungstates or borates occur, although the main phase still exists. A series of syntheses including adjustment of the calcining temperature and the holding time did not markedly improve the purity of the product, suggesting that Mo can not substitute for W completely. Once the doping amount of Mo^{6+} is up to a certain value, formation of the impurity is unavoidable. Figure 2 shows the enlarged XRD patterns from 28 to 29° of the samples $La_{2.7}BW_{1-x}Mo_xO_9$:$0.3Eu^{3+}$ (x = 0−0.3), respectively. In comparison with the diffraction peaks of the La_3BWO_9 host, the diffraction peaks of $La_{2.7}BW_{1-x}Mo_xO_9$:$0.3Eu^{3+}$ samples are found shifted toward the higher 2θ direction with an increase in the content of Mo^{6+}. It can be ascribed to the successful incorporation of Mo^{6+} into the lattice of $La_{2.7}BW_{1-x}Mo_xO_9$:$0.3Eu^{3+}$, which in turn leads to the shrinkage of unit cell volume, considering that the ionic radius of Mo^{6+} is smaller than that of W^{6+} (Mo^{6+}, 0.59 Å; W^{6+}, 0.60 Å).

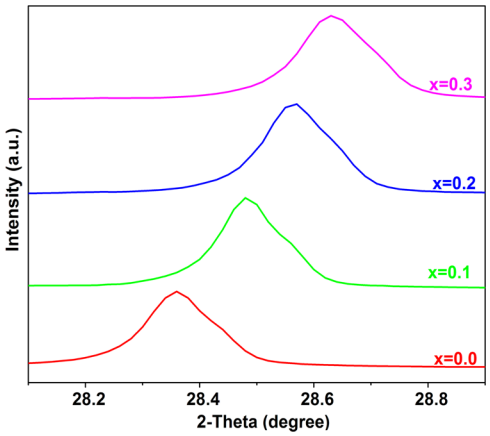

Figure 2. Enlarged XRD patterns from 28 to 29° of $La_{2.7}W_{1-x}Mo_xO_9$:$0.3Eu^{3+}$ (x = 0−0.3).

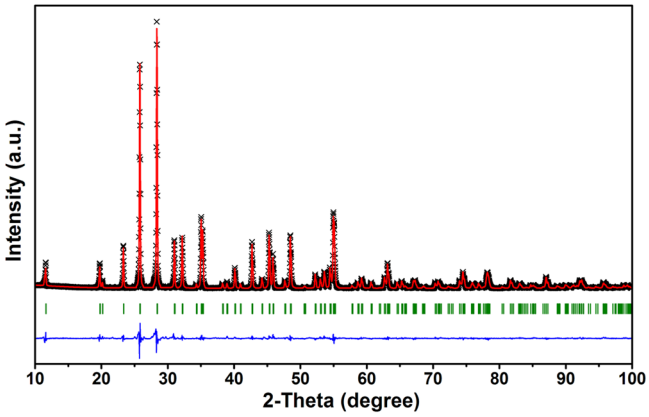

Figure 4. Rietveld refinement of the powder XRD patterns for $La_{2.7}BW_{0.7}Mo_{0.3}O_9$:$0.3Eu^{3+}$.

On the basis of XRD patterns, the lattice constants and atom positions of the samples $La_{2.7}BW_{1-x}Mo_xO_9$:$0.3Eu^{3+}$ (x = 0−0.3) are refined by the GSAS suite program of the Rietveld method[27] using La_3BWO_9 as the initial model (ICSD# 39809).[31] This series of materials crystallizes in a hexagonal structure with the $P6_3$ space group. As illustrated in Figure 3, W atoms in the structure are surrounded by six oxygen atoms, forming a trigonal-prismatic coordination, which shares edges with three rare-earth polyhedrons. La atoms adopt 9-fold coordination, of which six O atoms are derived from three WO_6 groups by sharing one edge with a WO_6 trigonal prism and the other three O atoms from BO_3 groups. LaO_9 polyhedrons

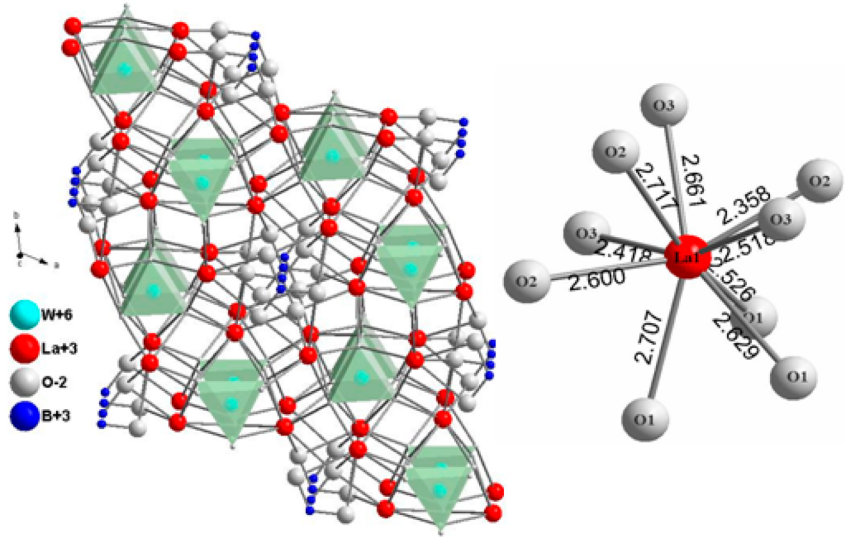

Figure 3. Crystal structure of the La_3BWO_9 host and the 9-fold coordination around La^{3+} ions.

dx.doi.org/10.1021/ic500748c | Inorg. Chem. 2014, 53, 9541−9547

Table 1. Crystallographic Details of $La_{2.7}W_{1-x}Mo_xO_9$:0.3Eu^{3+} (x = 0−0.3)

formula	a/b (Å)	c (Å)	V (Å^3)	R_{wp} (%)
$La_{2.7}BWO_9$:0.3Eu^{3+}	8.8140(1)	5.5628(1)	374.25(1)	12.0
$La_{2.7}BW_{0.9}Mo_{0.1}O_9$:0.3$Eu^{3+}$	8.8112(1)	5.5582(1)	373.71(1)	11.1
$La_{2.7}BW_{0.8}Mo_{0.2}O_9$:0.3$Eu^{3+}$	8.8105(1)	5.5487(1)	373.01(1)	12.6
$La_{2.7}BW_{0.7}Mo_{0.3}O_9$:0.3$Eu^{3+}$	8.8095(4)	5.5387(2)	372.26(1)	13.6

Table 2. Fractional Coordinates of $La_{2.7}BW_{0.7}Mo_{0.3}O_9$:0.3$Eu^{3+}$

atom	position	x/a	y/b	z/c	occ	U (Å^2)
W1/Mo1	2b	1/3	2/3	0.4170(1)	0.7/0.3	0.0063/0.02626
La1/Eu1	6c	0.3653(2)	0.08683(1)	0.3923(8)	0.9/0.1	0.0173/0.03386
O1	6c	0.1645(2)	0.04320(3)	1.039(3)	1	0.04841
O2	6c	0.1522(3)	0.4701(2)	0.1750(4)	1	0.03256
O3	6c	0.1742(2)	0.5404(3)	0.6120(5)	1	0.07386
B1	2a	0	0	0.2771(1)	1	0.009070

Table 3. Selected Bond Distances of $La_{2.7}BW_{0.7}Mo_{0.3}O_9$: 0.3$Eu^{3+}$

bond	distance (Å)	bond	distance (Å)	bond	distance (Å)
W1/Mo1−O2	2.138(2)	W1/Mo1−O3	1.675(2)	La1/Eu1−O2	2.274(2)
W1/Mo1−O2	2.138(2)	La1/Eu1−O1	2.534(2)	La1/Eu1−O2	2.361(2)
W1/Mo1−O2	2.138(2)	La1/Eu1−O1	2.688(2)	La1/Eu1−O3	2.604(3)
W1/Mo1−O3	1.675(2)	La1/Eu1−O1	2.622(2)	La1/Eu1−O3	2.604(3)
W1/Mo1−O3	1.675(2)	La1/Eu1−O2	2.996(2)	La1/Eu1−O3	2.657(2)

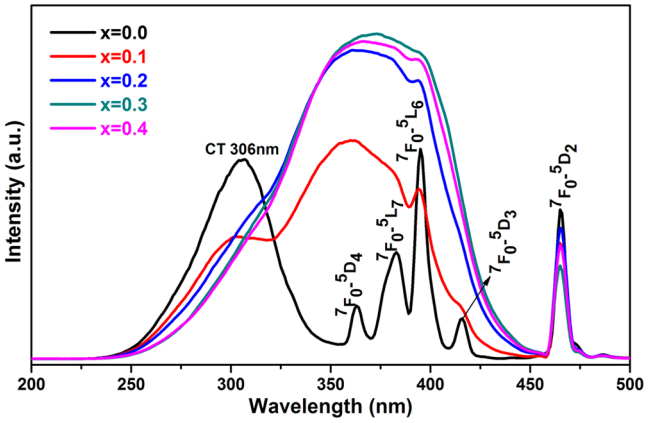

Figure 5. Excitation spectra of $La_{2.7}BW_{1-x}Mo_xO_9$:0.3Eu^{3+} monitored at 617 nm.

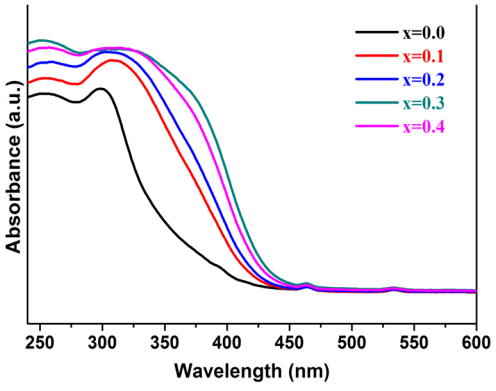

Figure 6. UV−vis absorption spectra of $La_{2.7}BW_{1-x}Mo_xO_9$:0.3Eu^{3+} (x = 0.1−0.4).

connect each other by sharing the corner O atoms of WO_6 and BO_3 groups, forming the framework of La_3BWO_9. When the

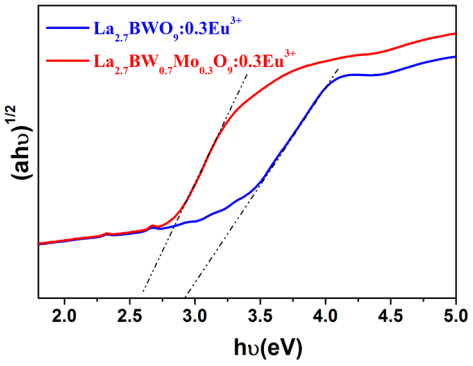

Figure 7. Calculated energy gap (E_{gap}) of $La_{2.7}BW_{1-x}Mo_xO_9$:0.3Eu^{3+} and $La_{2.7}BWO_9$:0.3Eu^{3+} from the UV−vis absorption spectra.

sample is doped with molybdenum, it uniformly substitutes W^{6+} at 2b sites, while Eu^{3+} ions enter the 6c sites of La^{3+}. The corresponding refinement profiles of $La_{2.7}BW_{0.7}Mo_{0.3}O_9$:0.3$Eu^{3+}$ are presented in Figure 4. The reliability factors of refinement on all observed reflections give satisfying results. Structural parameters and fractional coordinates of $La_{2.7}BW_{0.7}Mo_{0.3}O_9$:0.3$Eu^{3+}$ for x = 0−0.3 are summarized in Tables 1 and 2. From Table 1, it can be seen that with an increase in the Mo-substitution amount, the unit cell volume decreases from 374.25 to 372.26 Å^3. The unit cell volume of $La_3BW_{0.7}Mo_{0.3}O_9$ obtained from DFT calculations is 372.15 Å^3, indicating that the results obtained from DFT calculations agree well with those from XRD Rietveld refinement. Some W(Mo)−O and La(Eu)−O bond distances in the structure of $La_{2.7}BW_{0.7}Mo_{0.3}O_9$:0.3$Eu^{3+}$ from Rietveld refinement are given in Table 3. Maczka et al.[22] have demonstrated that, for europium in the middle of lanthanide boratotungstates, the differences between W(Mo)−O2 and W(Mo)−O3 bond distances are enlarged, leading to a significant asymmetry (distortion) of WO_6 polyhedra in the Ln_3BWO_9 compounds, which is responsible for the optical

dx.doi.org/10.1021/ic500748c | Inorg. Chem. 2014, 53, 9541−9547

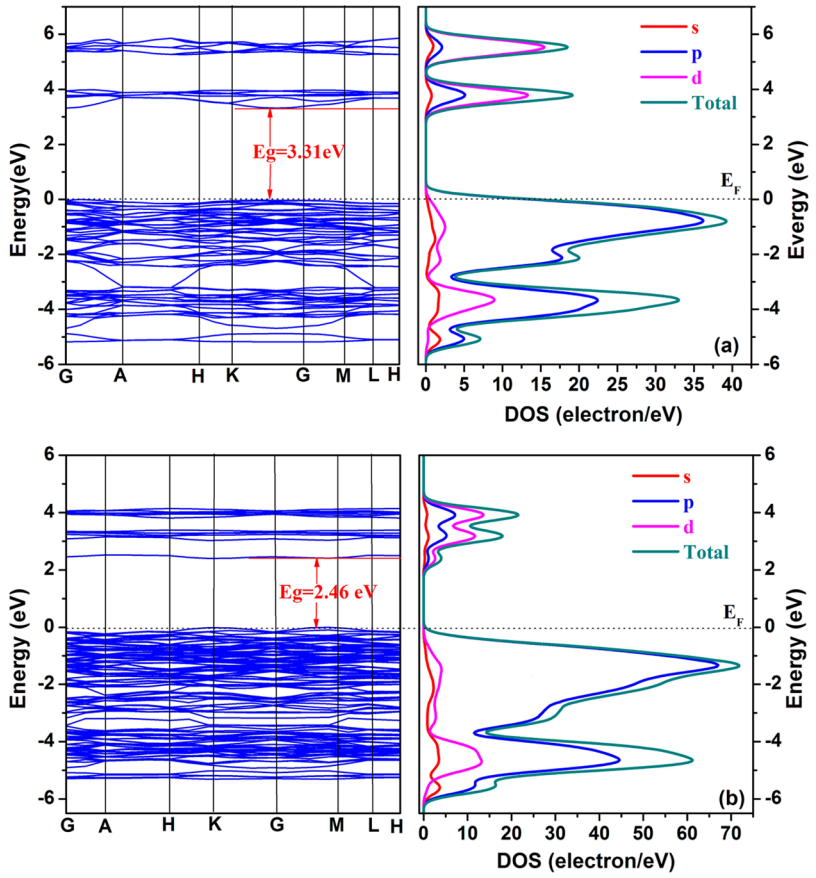

Figure 8. Calculated band structures (left) and DOSs (right) of La_3BWO_9 and $La_3BW_{0.7}Mo_{0.3}O_9$ near the Fermi energy (E_F) level. The Fermi energy is the 0 of the energy scale. E_g is the calculated forbidden band gap of the ground state of the system.

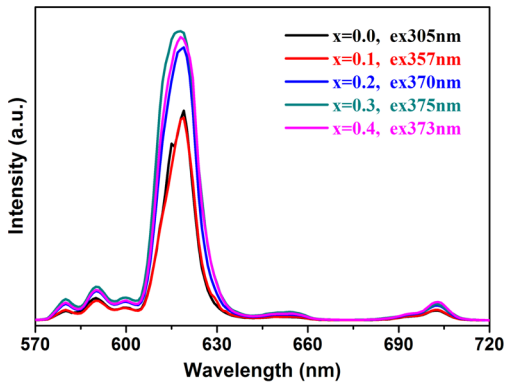

Figure 9. Emission spectra of $La_{2.7}BW_{1-x}Mo_xO_9$:0.3Eu^{3+} (x = 0–0.4) monitored at the hypersensitive excitation, respectively.

nonlinearity of Ln_3BWO_9 compounds. From Table 3 it can been seen that the discrepancy between the W(Mo)–O2 and W(Mo)–O3 bond distances in $La_{2.7}BW_{0.7}Mo_{0.3}O_9$: 0.3$Eu^{3+}$ is up to 0.46 Å, where the shortest and the longest W–O bonds in La_3BWO_9 are 1.922 and 1.956 Å, respectively (the difference is only 0.024 Å). This difference may arise from the two effects of Mo^{6+} substitution for W^{6+} and Eu^{3+} substitution for La^{3+}.

3.2. Excitation and UV–Vis Absorption Spectra. Figure 5 shows the excitation spectra of $La_{2.7}BW_{1-x}Mo_xO_9$:0.3Eu^{3+} with different doping amounts of Mo^{6+} monitored at the $^5D_0$–$^7F_2$ transition of 617 nm. The excitation spectra of $La_{2.7}BW_{1-x}Mo_xO_9$:0.3Eu^{3+} without doping of Mo^{6+} ions consists of two parts. The intense and broad band of 230–350 nm maximized at 306 nm is ascribed to charge transfer from the ligand to the metal (LMCT), derived from the $^1T_1$–$^1A_1$ transition of $O^{2-} \rightarrow W^{6+}$ in the WO_6 group and charge transfer of $O^{2-} \rightarrow Eu^{3+}$.[32] The sharp peaks between 360 and 500 nm are assigned to the characteristic transition of Eu^{3+} within its $4f^6$ configuration. Five of these sharp excitations are observed at 363 nm ($^7F_0$–$^5D_4$), 383 nm ($^7F_0$–$^5L_7$), 395 nm ($^7F_0$–$^5L_6$), 416 nm ($^7F_0$–$^5D_3$), and 465 nm ($^7F_0$–$^5D_2$).[28] When Mo^{6+} ions are incorporated into the lattice, the characteristic sharp lines of the excitation spectra of Eu^{3+} monitored at 617 nm are prominently enhanced, which join the LMCT band into a broad band ranging from 250 to 450 nm centered at 375 nm. In the meantime, the LMCT band around 306 nm decreases and shifts toward longer wavelength. These features are advantageous for near-UV or blue GaN-based LED applications. When the content of Mo^{6+} ions increases to x = 0.3, the intensity of the broad excitation band reaches the maximum.

UV–vis absorption spectra of $La_{2.7}BW_{1-x}Mo_xO_9$:0.3Eu^{3+} (x = 0–0.4) in Figure 6 exhibit the same change as excitation spectra. It is observed that all of the samples have strong absorption of near-UV light. With increasing Mo content, the absorption edge of the $La_{2.7}BW_{1-x}Mo_xO_9$:0.3Eu^{3+} series red shifts gradually, which indicates the variation of the band gap. As is well-known, the absorption coefficient α of a semiconductor oxide and its band gap energy E_{gap} are related through the equation

$$(\alpha h\nu)^{1/2} \propto (h\nu - E_{gap}) \quad (1)$$

dx.doi.org/10.1021/ic500748c | Inorg. Chem. 2014, 53, 9541–9547

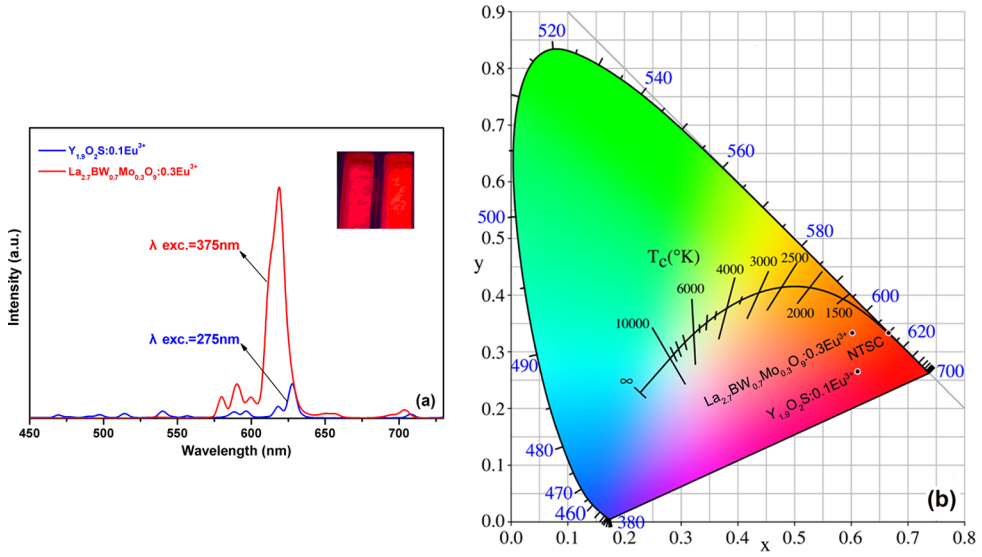

Figure 10. Photoluminescence (a) and CIE coordinate (b) comparison between $La_{2.7}BW_{0.7}Mo_{0.3}O_9$:0.3$Eu^{3+}$ and the commercial red phosphor $Y_{1.9}O_2S$:0.1Eu^{3+} under their respective hypersensitive excitations of 375 and 275 nm. The inset of (a) is the fluorescence image under 365 nm excitation.

where h is Planck's constant and ν is the frequency of the light. From a plot of this equation derived from the UV−vis absorption spectra, the energy gap (E_{gap}) of a semiconductor oxide can be estimated.[14,33] From Figure 7, the absorption edges of indirect transition for samples of x = 0 and x = 0.3 are observed to be 2.93 and 2.55 eV, which are slightly smaller than the DFT predicted values by 0.2−0.4 eV. The absorption of WO_6/MoO_6 groups is ascribed to the optical excitation of electrons from the valence band (VB) to the conductive band (CB).[34] The calculated band structure in Figure 8 reveals that the hexagonal La_3BWO_9 and the Mo^{6+}-doped sample of $La_{2.7}BW_{0.7}Mo_{0.3}O_9$ are direct band gap materials. Orbital population analysis of DFT calculations shows that the tops of the VBs are identically dominated by the 2p orbitals of O atoms. The CBs are separated into two parts: the upper energy parts are contributed by La 5d orbitals, and the lower parts are formed mainly by W 5d and Mo 4d orbitals, respectively. When Figure 8b is compared with Figure 8a, it can be seen that, with Mo^{6+} doping, orbitals of O 2p and orbitals of W 5d and Mo 4d at the bottom of the VBs are broadened, suggesting some interband forms as a result of charge transfer from O 2p to W 5d and Mo 4d orbitals.[35] In the structure of $La_3BW_{1-x}Mo_xO_9$, the three-dimensional arrangement of WO_6 is separated by LaO_9. The replacement of Mo for W increases the distance between WO_6 groups and enlarges the electron delocalization within each $W(Mo)O_6$ group. Rietveld structure refinements verify that the difference between the W(Mo)−O2 and W(Mo)−O3 bond distances in $W(Mo)O_6$ polyhedra are enlarged due to the two effects of Mo^{6+} substitution for W^{6+} and Eu^{3+} substitution for La^{3+}. The distorted or asymmetric $W(Mo)O_6$ polyhedra are also responsible for this delocalization, In addition, the electronegativity of Mo (2.16) is lower than that of W (2.36). The electron cloud overlaps between center cations (W^{6+}/ Mo^{6+}) and their coordination anions (O^{2-}) are enlarged,[25] and the charge transfer from O to W/Mo easily occurs, which directly results in a decrease of the energy gap. A lower excitation energy will lead to the charge transfer. Therefore, the red shift of the LMCT band was observed. Meanwhile, in the structure of La_3BWO_9, the distance between WO_6 groups is short. Almost all absorbed energy from WO_6 is quenched in the transferring process along the WO_6 framework and only a small amount of energy is trapped by Eu^{3+}. With an increase in Mo content, the concentration of the WO_6 group is diluted, the distance between WO_6 group becomes longer, and the energy transition is blocked by MoO_6, which result in more energy transferred from the host to Eu^{3+} ions.[36]

3.3. Photoluminescence Properties and Surroundings of Eu^{3+}. Figure 9 shows the room-temperature emission spectra of the as-prepared $La_{2.7}BW_{1-x}Mo_xO_9$:0.3Eu^{3+} (x = 0−0.4). The emission peaks are ascribed to the characteristic $^5D_0-^7F_J$ (J = 1−4) transitions of Eu^{3+} ions and the hypersensitive emission located at 617 nm ($^5D_0-^7F_2$). It can be observed that. with an increase in Mo^{6+} content, the excitation is shifted to longer wavelengths and the hypersensitive emission of $^5D_0-^7F_2$ is enhanced and reaches a maximum when x = 0.3. It is known that the 4f energy levels of Eu^{3+} are hardly affected by the crystal field because of the shielding effect of $5s^25p^6$ electrons. Therefore, there is no remarkable shift in the positions of the emission peaks in comparison with those of other Eu^{3+}-doped systems. On the other hand, Eu^{3+} emission is sensitive to the local chemical environment in terms of Judd−Ofelt theory.[37,38] If Eu^{3+} resides in sites with an inversion center, the $^5D_0-^7F_1$ magnetic dipole transition is dominant, while in a site without an inversion center, the $^5D_0-^7F_2$ electric-dipole transition is prominent.[36] The integrated intensity ratio of $R = I(^5D_0-^7F_2)/I(^5D_0-^7F_1)$ is considered as an indication of the asymmetry of the coordination polyhedron of Eu^{3+}.[39] In the $La_{2.7}BW_{1-x}Mo_xO_9$:0.3Eu^{3+} hexagonal cell, Eu^{3+} ion was thought to substitute for the La^{3+} site, which has 9-fold coordination with O atoms, with a C_1 point symmetry. Obviously, with an increase of the incorporation amount of Mo^{6+}, the emission derived from $^5D_0-^7F_J$ is enhanced systematically and the R value increases. This results in a weakening centrosymmetry of the site where Eu^{3+} ions locate and an efficient energy transfer from the host to the Eu^{3+} activator.

Figure 10 shows a comparison of the emission spectra and the fluorescence images between $La_{2.7}BW_{0.7}Mo_{0.3}O_9$:0.3$Eu^{3+}$ and the commercial red phosphor $Y_{1.9}O_2S$:0.1Eu^{3+} at their

dx.doi.org/10.1021/ic500748c | Inorg. Chem. 2014, 53, 9541−9547

hypersensitive excitations of 375 and 275 nm, respectively. Under the same measurement conditions, the emission intensity of $La_{2.7}BW_{0.7}Mo_{0.3}O_9$:0.3$Eu^{3+}$ phosphor is over 6 times stronger than that of the commercial red phosphor, indicating that this phosphor could be applied to near-UV LED chips with high luminance. The corresponding CIE color coordinates is about (0.603, 0.333), slightly deviating from the standard NTSC (0.670, 0.330) red to orange. With a tuned and broadened excitation wavelength, $La_{2.7}BW_{0.7}Mo_{0.3}O_9$:0.3$Eu^{3+}$ may find promising application in near-UV LEDs as a red phosphor.

4. CONCLUSION

Novel high-efficiency red phosphors $La_{2.7}BW_{1-x}Mo_xO_9$:Eu^{3+} (x = 0−0.4) have been prepared by introducing Mo^{6+} into the WO_6 lattice via solid-state reactions. The phase structure, UV−vis absorption spectra, and photoluminescence properties were studied as a function of the Mo/W ratio. Both the electronic structure and absorption spectra indicated that, with Mo^{6+} introduced into the lattice, the band gap of $La_3BW_{1-x}Mo_xO_9$ became narrower than that of La_3BWO_9. Accordingly, the excitation spectra shifted to longer wavelengths, which is advantageous for phosphors to match with commercially available near-UV LED chips. The red emission of $La_{2.7}BW_{1-x}Mo_xO_9$:0.3Eu^{3+} phosphor was improved by 30% at x = 0.3 under the excitation of the broad band without loss of color purity. The Rietveld refinement results indicated that replacement of Mo for W reached a maximum at about 30%. The band structure and orbital population analysis by density functional theory calculations revealed that the hexagonal La_3BWO_9 and $La_3BW_{0.7}Mo_{0.3}O_9$ were direct bandgap materials, and the near-UV excitations were due to the electronic transitions from the O 2p orbitals to W 5d and Mo 4d orbitals, respectively. Using Mo^{6+} to substitute W^{6+} to adjust the LMCT band of the tungstate host toward the near-UV region may represent a facile route to modulate a matchable excitation wavelength and produce an effective luminescence enhancement of Eu^{3+} for LED applications because of the isomorphism effect.

■ ASSOCIATED CONTENT

Supporting Information

A figure giving the calculated energy gap (E_{gap}) for samples of $La_{2.7}BW_{1-x}Mo_xO_9$:0.3Eu^{3+} (x = 0−0.3). This material is available free of charge via the Internet at http://pubs.acs.org.

■ AUTHOR INFORMATION

Corresponding Author

*E-mail for J.H.: hjinping@shnu.edu.cn.

Notes

The authors declare no competing financial interest.

■ ACKNOWLEDGMENTS

This work was supported by the Program of Shanghai Normal University (DZL124).

■ REFERENCES

(1) Pimputkar, S.; Speck, J. S.; DenBaars, S. P.; Nakamura, S. *Nat. Photonics* **2009**, *3*, 180−182.
(2) Tonzani, S. *Nature* **2009**, *459*, 312−314.
(3) Denbaars, S. P.; Feezell, D.; Kelchner, K.; Pimputkar, S.; Pan, C.-C.; Yen, C.-C.; Tanaka, S.; Zhao, Y.; Pfaff, N.; Farrell, R.; Iza, M.; Keller, S.; Mishra, U.; Speck, J. S.; Nakamura, S. *Acta Mater.* **2013**, *61*, 945−951.
(4) Ponce, F. A.; Bour, D. P. *Nature* **1997**, *386*, 351−359.
(5) Nakamura, S. *III-Vs Rev.* **1998**, *11*, 22−26.
(6) Jia, L.; Shao, Z.; Lü, Q.; Tian, Y.; Han, J. *Ceram. Int.* **2014**, *40*, 739−743.
(7) Zhang, X.; Zhang, J.; Gong, M. *Opt. Mater.* **2014**, *36*, 850−853.
(8) Axe, J. D.; Weller, P. F. *J. Chem. Phys.* **1964**, *40*, 3066−3069.
(9) Guo, Y.; Sun, M.; Guo, W.; Ren, F.; Chen, D. *Opt. Laser Technol.* **2010**, *42*, 1328−1331.
(10) Jin, H.; Wu, H.; Tian, L. *J. Lumin.* **2012**, *132*, 1188−1191.
(11) Tian, L.; Yang, P.; Wu, H.; Li, F. *J. Lumin.* **2010**, *130*, 717−721.
(12) Dutta, P. S.; Khanna, A. *ECS J. Solid State Sci. Technol.* **2012**, *2*, R3153−3167.
(13) Huang, J.; Luo, H.; Zhou, P.; Yu, X.; Li, Y. *J. Lumin.* **2007**, *126*, 881−885.
(14) Li, H.; Yang, H. K.; Moon, B. K.; Choi, B. C.; Jeong, J. H.; Jang, K.; Lee, H. S.; Yi, S. S. *Inorg. Chem.* **2011**, *50*, 12522−12530.
(15) Neeraj, S.; Kijima, N.; Cheetham, A. K. *Chem. Phys. Lett.* **2004**, *387*, 2−6.
(16) Neeraj, S.; Kijima, N.; Cheetham, A. K. *Solid State Commun.* **2004**, *131*, 65−69.
(17) Li, H.; Yang, H. K.; Moon, B. K.; Choi, B. C.; Jeong, J. H.; Jang, K.; Lee, H. S.; Yi, S. S. *J. Alloys Compd.* **2011**, *509*, 8788−8793.
(18) Dai, P.; Zhang, X.; Li, X.; Wang, G.; Zhao, C.; Liu, Y. *J. Lumin.* **2011**, *131*, 653−656.
(19) Huang, Y.; Seo, H. J. *Mater. Lett.* **2012**, *84*, 107−109.
(20) Zhu, R.; Huang, Y.; Seo, H. J. *J. Electrochem. Soc.* **2010**, *157*, H1116−1120.
(21) Krut'ko, V. A.; Belik, A. A.; Lysanova, G. V. *Russ. Inorg. Chem.* **2006**, *51*, 884−889.
(22) Mączka, M.; Tomaszewski, P.; Stępień-Damm, J.; Majchrowski, A.; Macalik, L.; Hanuza, J. *J. Solid State Chem.* **2004**, *177*, 3595−3602.
(23) Gokhman, L. Z.; Dzhurinskii, B. F.; Efremov, V. A.; Ilyukhin, A. B.; Chistova, V. I. *Zh. Neorg. Khim.* **1994**, *39*, 1075.
(24) Bandurkin, G. A.; Lysanova, G. V.; Krut'ko, V. A.; Chudinova, N. N.; Komova, M. G. *Russ. Inorg. Chem.* **2009**, *54*, 572.
(25) Zhang, L.; Lu, Z.; Han, P.; Wang, L.; Zhang, Q. *J. Mater. Chem. C* **2013**, *1*, 54−57.
(26) Segall, M. D.; Philip, J. D. L.; Probert, M. J.; Pickard, C. J.; Hasnip, P. J.; Clark, S. J.; Payne, M. C. *J. Phys.: Condens. Matter.* **2002**, *14*, 2717−2744.
(27) Larson, A. C.; Von Dreele, R. B. *Los Alamos National Laboratory Report LAUR*; Los Alamos National Laboratory: Los Alamos. NM, 2004; pp 86−748.
(28) Monkhorst, H. J.; Pack, J. D. B. *Phys. Rev.* **1976**, *13*, 5188−5192.
(29) Ceperley, D. M.; Alder, B. *J. Phys. Rev. Lett.* **1980**, *45*, 566−569.
(30) Perdew, J. P.; Zunger, A. *Phys. Rev. B* **1981**, *23*, 5048.
(31) Gokhman, L. Z.; Dzhurinskii, B. F.; Efremov, V. A.; Ilyukhin, A. B.; Chistova, V. I. *Zh. Neorg. Khim.* **1994**, *39*, 1075−1079.
(32) Yiguo Su, L. L.; Guangshe, Li. *Chem. Mater.* **2008**, *20*, 6060−6067.
(33) Chang, W.-T.; Hsueh, Y.-C.; Huang, S.-H.; Liu, K.-I.; Kei, C.-C.; Perng, T.-P. J. *J. Mater. Chem. A* **2013**, *1*, 1987−1991.
(34) Ye, S.; Wang, C. H.; Liu, Z. S.; Lu, J.; Jing, X. P. *Appl. Phys. B: Laser Opt.* **2008**, *91*, 551−557.
(35) Blasse, G.; Bril, A. *J. Chem. Phys.* **1966**, *45*, 2350−2355.
(36) Dexter, D. L. *J. Chem. Phys.* **1954**, *22*, 1063−1070.
(37) Jia, G.; Tu, C.; Li, J.; You, Z.; Zhu, Z.; Wu, B. *Inorg. Chem.* **2006**, *45*, 9326−9331.
(38) Liu, C.; Liu, J. *J. Phys. Chem. B* **2006**, *110*, 20277−20281.
(39) Bleier, G. C.; Nyman, M.; E.S. Rohwer, L.; Rodriguez, M. A. *J. Solid State Chem.* **2011**, *184*, 3221−3227.